



## Controllable synthesis of cerium zirconium oxide nanocomposites and their application for photocatalytic degradation of sulfonamides

Peishen Li<sup>a</sup>, Ming Guo<sup>a</sup>, Qiang Wang<sup>a,\*</sup>, Zhen Li<sup>a</sup>, Changzheng Wang<sup>b,\*</sup>, Ning Chen<sup>a</sup>, Chong-Chen Wang<sup>b,\*</sup>, Chongqing Wan<sup>a</sup>, Shaowei Chen<sup>c,\*</sup>

<sup>a</sup> Laboratory for Micro-sized Functional Materials & College of Elementary Education and Department of Chemistry, Capital Normal University, Beijing, 100048, PR China

<sup>b</sup> Beijing Key Laboratory of Functional Materials for Building Structure and Environment Remediation, Beijing University of Civil Engineering and Architecture, Beijing 100044, PR China

<sup>c</sup> Department of Chemistry and Biochemistry, University of California, Santa Cruz, CA 95064, USA



### ARTICLE INFO

**Keywords:**  
Ce<sub>x</sub>Zr<sub>y</sub>O<sub>2</sub>  
Nanocomposite  
Photodegradation  
Sulfonamides  
Mechanism

### ABSTRACT

In this work, series of cerium zirconium oxide (Ce<sub>x</sub>Zr<sub>y</sub>O<sub>2</sub>) nanocomposites were successfully synthesized through a facile hydrothermal method, and their photocatalytic sulfonamide performances were investigated. Scanning electron microscopy and transmission electron microscopy measurements demonstrated that the size of the Ce<sub>x</sub>Zr<sub>y</sub>O<sub>2</sub> nanocomposites increased with the increasing Zr content. The Ce element in the Ce<sub>x</sub>Zr<sub>y</sub>O<sub>2</sub> nanocomposites existed mainly in the forms of Ce<sup>3+</sup> and Ce<sup>4+</sup>, and the Zr element in the form of Zr<sup>4+</sup>. Additionally, UV-vis diffuse reflectance spectroscopy, transient photocurrent, electrochemical impedance spectroscopy and electron spin resonance measurements showed that among the series, the Ce<sub>0.9</sub>Zr<sub>0.1</sub>O<sub>2</sub> sample exhibited the smallest band gap, the largest photoelectric response and lowest impedance. Under the illumination of artificial solar light, the Ce<sub>0.9</sub>Zr<sub>0.1</sub>O<sub>2</sub> composite showed the best photocatalytic performance with a degradation efficiency of 91.33% within 30 min, which was largely ascribed to the efficient production of 'O<sub>2</sub>' and 'OH' radicals.

### 1. Introduction

As antibiotics are used enormously every year in the world, the pollution of antibiotics in water has become a serious environmental issue [1,2]. Among these, sulfonamides-based antibiotics are persistent and complex in structure, which can hinder bacterial growth or even kill bacteria [3]. Thus far, a variety of techniques have been developed to degrade sulfonamides in water, such as adsorption, advanced oxidation, biodegradation, and photocatalytic degradation [1,4,5]. Of these, photocatalytic degradation is generally considered to be the most effective method for the removal of antibiotics [6]. With the rapid progress of nanomaterials chemistry, nanoscale photocatalysts have been attracting extensive attention for their low cost and high stability [7–12].

Traditional wastewater treatment has a low removal rate of sulfonamides. Therefore, there is an urgent need to develop more effective technologies to eliminate sulfonamides and other antibiotics [13]. Advanced oxidation process (AOP) is a promising strategy, which can also be used as an alternative strategy for industrial wastewater treatment. Among the various AOPs, heterogeneous photocatalysis driven by solar

energy has the advantages of high efficiency, low cost, and minimal environmental impacts, and thus is a viable method to remove antibiotics [14–16]. In fact, photocatalysis has been widely used to convert a wide range of refractory antibiotics to readily biodegradable compounds, and eventually mineralize them to innocuous carbon dioxide and water [17–20]. For instance, Kim et al. [21] investigated the degradation pathway of sulfa antibiotics in dielectric barrier discharge plasma systems. Song et al. [22] studied the degradation of sulfonamides by graphitic carbon nitride (g-C<sub>3</sub>N<sub>4</sub>) under visible light photo-irradiation. Di et al. [23] evaluated the visible-light degradation of sulfonamides by Z-schemed ZnO/g-C<sub>3</sub>N<sub>4</sub> heterojunctions with amorphous Fe<sub>2</sub>O<sub>3</sub> as an electron mediator. Latha et al. observed enhanced visible light photocatalytic activity of CeO<sub>2</sub>/alumina nanocomposites by facile mixing-calcination method for dye degradation [24]. Hao et al. observed enhanced photocatalytic degradation with a multilayer open structure of dendritic crosslinked CeO<sub>2</sub>-ZrO<sub>2</sub> composites [25]. In fact, a large number of nanostructured materials and nanocomposites have been employed for the remediation of a range of sulfonamide pollutants [26].

However, to the best of our knowledge, studies have been scarce of

\* Corresponding authors.

E-mail addresses: [qwchem@gmail.com](mailto:qwchem@gmail.com) (Q. Wang), [changzhwang@163.com](mailto:changzhwang@163.com) (C. Wang), [wangchongchen@bucea.edu.cn](mailto:wangchongchen@bucea.edu.cn) (C.-C. Wang), [shaowei@ucsc.edu](mailto:shaowei@ucsc.edu) (S. Chen).

the photocatalytic application of cerium-zirconium oxide composites ( $\text{Ce}_x\text{Zr}_y\text{O}_2$ ) towards the photodegradation of sulfonamides [6,27–29]. In this work,  $\text{Ce}_x\text{Zr}_y\text{O}_2$  nanocomposites were synthesized at different Ce:Zr molar ratios by a simple hydrothermal method and exhibited apparent photocatalytic activity towards the degradation of sulfonamides.

## 2. Experimental

### 2.1. Chemicals

All chemicals were purchased from Alfa Aesar and used as received without any further purification.

### 2.2. Preparation of $\text{Ce}_x\text{Zr}_y\text{O}_2$ nanocomposites

$\text{Ce}_x\text{Zr}_y\text{O}_2$  nanocomposites were synthesized via a facile hydrothermal method at the Ce:Zr molar feed ratio of 9:1, 7:1, 5:1, 3:1, and 1:1. Experimentally, a calculated amount of cerium nitrate ( $\text{Ce}(\text{NO}_3)_3 \cdot 6\text{H}_2\text{O}$ ) and zirconium nitrate ( $\text{Zr}(\text{NO}_3)_4 \cdot 5\text{H}_2\text{O}$ ) were mixed in a 200 mL beaker, into which was then added 70 mL of deionized water to fully dissolve the reagents under magnetic stirring. The total amount of  $\text{Ce}(\text{NO}_3)_3 \cdot 6\text{H}_2\text{O}$  and  $\text{Zr}(\text{NO}_3)_4 \cdot 5\text{H}_2\text{O}$  was kept at 5 mmol among the samples. 200 mmol of urea was then added to each solution under magnetic stirring for 1 h to facilitate the reaction. The resulting suspension was then transferred to a 100 mL Teflon-lined autoclave, which was sealed and heated at 373 K for 10 h. After the autoclaves were cooled down to room temperature, the resulting light yellow precipitates were collected and washed several times with distilled water and absolute ethanol, and dried at 333 K for 4 h. The dried samples were then calcined in a muffle furnace at 673 K for 5 h, affording the  $\text{Ce}_x\text{Zr}_y\text{O}_2$  nanocomposites [30].

### 2.3. Characterizations

The morphology of the obtained samples was measured by scanning electron microscopy (SEM, Hitachi S4800) and high-resolution transmission electron microscopy (HRTEM, JEOL 2010 F), where the lattice fringes and the corresponding selected-area electron diffraction (SAED) patterns were obtained. Powder X-ray diffraction (XRD) patterns were acquired with a Bruker D8 diffractometer with  $\text{Cu K}_\alpha$  radiation ( $\lambda = 1.5418 \text{ \AA}$ ). X-ray photoelectron spectroscopy (XPS) measurements were performed with an ESCALAB 250 with  $\text{Al K}_\alpha$  radiation. Binding energies were calibrated against carbon (C 1s, 284.8 eV). Semiquantitative analysis of atomic ratio was obtained by using the integrated peak areas in energy dispersive X-ray spectroscopy (EDS) measurements. Generation of superoxide and hydroxyl radicals was analyzed under visible light irradiation via electron spin resonance (ESR, ER200-SRC-10/12) measurements. Electrochemical impedance spectra (EIS) and transient photocurrents were acquired with a CHI760E electrochemical workstation. Specific surface areas of the prepared samples were determined by a multipoint Brunauer-Emmett-Teller (BET) analysis of the nitrogen adsorption and desorption isotherms at liquid nitrogen temperature recorded on an Autosorb-1 apparatus. Prior to analysis, the samples were heated at 120 °C in vacuum for 6 h. Optical absorbance and UV-vis diffuse reflectance spectra (DRS) were measured with a UV-vis Spectrophotometer (UV-2600, Thermo, Japan). The average intensity of the light source was determined by an optical power meter (PM100D, THORLARBS). Fluorescence measurements were carried out with an Edinburgh FLS900 instrument. Mass spectrometry measurements were performed with a Thermo Scientific Q Exactive/Focus LC-MS/MS /Ultimate 3000 UPLC instrument.

### 2.4. Photocatalysis

Sulfonamide was used as an illustrating example to evaluate the

photocatalytic performance of  $\text{Ce}_x\text{Zr}_y\text{O}_2$  nanocomposites towards antibiotics. A customized artificial solar light photo-reactor equipped with a 300 W xenon lamp (FX300, PerfectLight) was employed as the light source. In a typical experiment, 5 mg of the  $\text{Ce}_x\text{Zr}_y\text{O}_2$  nanocomposites prepared above was added into a quartz tube containing 50 mL of a sulfonamide ( $10 \text{ mg L}^{-1}$ ) solution [16], and stirred for 60 min in the dark to reach an adsorption-desorption equilibrium. The photocatalytic activity of  $\text{CeO}_2$  and  $\text{ZrO}_2$  alone was studied as well. The xenon lamp was switched on to initiate the photocatalytic reaction for 30 min. At regular time intervals, 1 mL aliquots were withdrawn and filtered by high-speed centrifugation immediately to remove the  $\text{Ce}_x\text{Zr}_y\text{O}_2$  nanocomposites. The concentration of sulfonamide in the test samples was analyzed using an UV-vis spectrophotometer by monitoring its maximum absorption at 257 nm [31]. The effect of initial pH (3, 6, 7 and 10) was studied and the pH was carefully adjusted with 0.1 M HCl and 0.2 M NaOH. The formation of radicals in the photocatalytic process was investigated using isopropanol (IPA), ethylenediamine tetraacetic acid disodium salt (EDTA-2Na) and benzoquinone (BQ) as scavengers (0.5 mM).

To quantify the apparent quantum efficiency (AQE) during the sulfonamide photodegradation, several bandpass filters (fwhm = 15 nm) were used to produce incident light at different wavelengths with a 300 W xenon lamp (Fx300, Perfect Light). For full spectrum measurements, the xenon lamp with a standard AM 1.5 g filter was used as the radiation source, and the output optical density was  $100 \text{ MW cm}^{-2}$ . In addition, the fluorescence intensity of  $\cdot\text{OH}$  concentration during photocatalytic degradation of sulfonamide was measured. Intermediates were further analyzed using a Thermo Scientific Q Exactive/Focus LC-MS/MS coupled to an Ultimate 3000 UPLC instrument quadrupole mass spectrometry, which was equipped with an Electrospray ionization (ESI) source. Separation was carried out with a  $100 \text{ m} \times 2.1 \text{ mm}$  Kinetex 2.6  $\mu\text{m}$  C18 column. The flow rate was set at  $0.2 \text{ mL min}^{-1}$ , injection volume 5 mL, test temperature 30 °C, wavelength 270/230/255 nm, solution A: 0.1% formic acid in ethanol, and solution B: 0.1% formic acid in water. Gradient elution: initial 5% A, 15 min, 50% B; 20 min, 50% B; 20.1 min, 50% B, 5.9 min, 26 min back to 5%, 2 min to balance the column. Mass spectrometric (MS) measurements were carried out in electrospray ionization (ESI) mode with jet positive and negative ionization: atomizer gas  $15 \text{ L min}^{-1}$ , sheath gas  $40 \text{ L min}^{-1}$ , capillary voltage 3200 V at 300 °C, and S lens RF level 50 V [16].

### 2.5. Density functional theory calculations

Density functional theory (DFT) calculations were performed by using the Vienna Ab-initio Simulation Package (VASP) [32]. The Perdew-Burke-Ernzerhof (PBE) functional [33,34] was employed to describe the exchange and correlation effect. The cutoff energy was set to 450 eV.

## 3. Results and discussion

### 3.1. Characterization and analysis

The morphology and size distribution of the  $\text{Ce}_x\text{Zr}_y\text{O}_2$  nanocomposites were first examined by SEM measurements. From Fig. 1, it can be seen that the change of the Ce:Zr molar ratio from 9:1 to 1:1 did not lead to a significant morphological variation of the  $\text{Ce}_x\text{Zr}_y\text{O}_2$  nanocomposites, which all consisted of clusters of nanoparticles (Fig. 1a–e). Yet, from Fig. 1f–j, the average size of the  $\text{Ce}_x\text{Zr}_y\text{O}_2$  nanoparticles can be seen to increase with increasing Zr loading, from 80 nm at Ce:Zr = 9:1 to 140 nm at Ce:Zr = 1:1. In fact, the percentage of nanoparticles larger than 100 nm increased from 20% at Ce:Zr = 9:1 to 90% at Ce:Zr = 1:1, and clustering of nanoparticles became increasingly apparent [35].

Fig. 2 shows representative TEM and HRTEM images of the as-prepared  $\text{Ce}_x\text{Zr}_y\text{O}_2$  nanocomposites at varied Ce:Zr molar ratios. It can

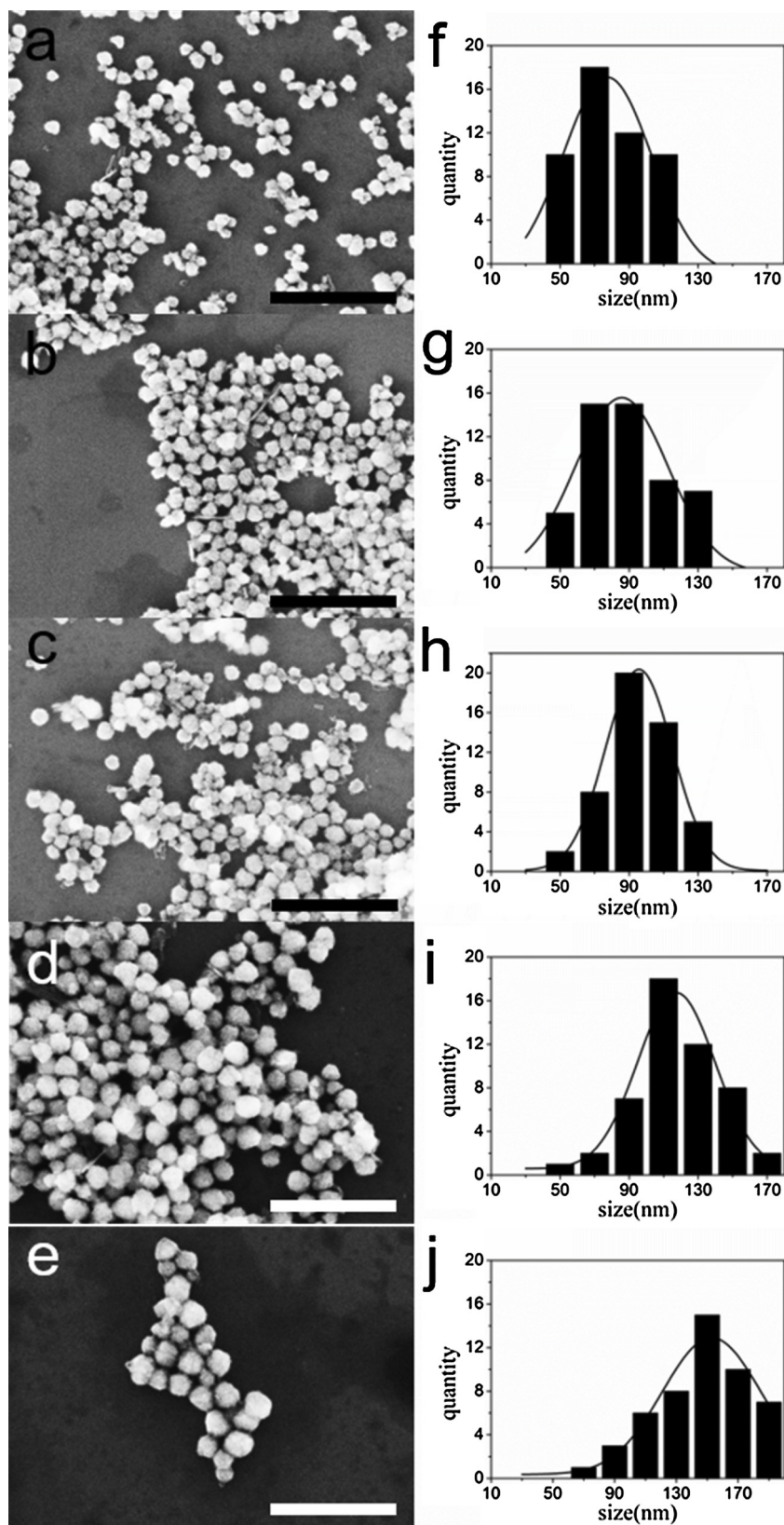


**Fig. 1.** (a–e) SEM images and (f–j) the corresponding size histograms of  $\text{Ce}_x\text{Zr}_y\text{O}_2$  nanocomposites prepared at different Ce/Zr molar ratios: (a) 9:1, (b) 7:1, (c) 5:1, (d) 3:1 and (e) 1:1. The scale bars in (a–e) are all 500 nm.

be found that the morphologies and sizes of the  $\text{Ce}_x\text{Zr}_y\text{O}_2$  nanocomposites (Fig. 2a–e) were in good agreement with those from SEM characterizations (Fig. 1). The internal void space in the  $\text{Ce}_x\text{Zr}_y\text{O}_2$

nanocomposites indicated large specific surface areas, which might be beneficial to increase accessibility of the  $\text{Ce}_x\text{Zr}_y\text{O}_2$  nanocomposites to sulfonamide molecules and facilitate their photocatalytic degradation

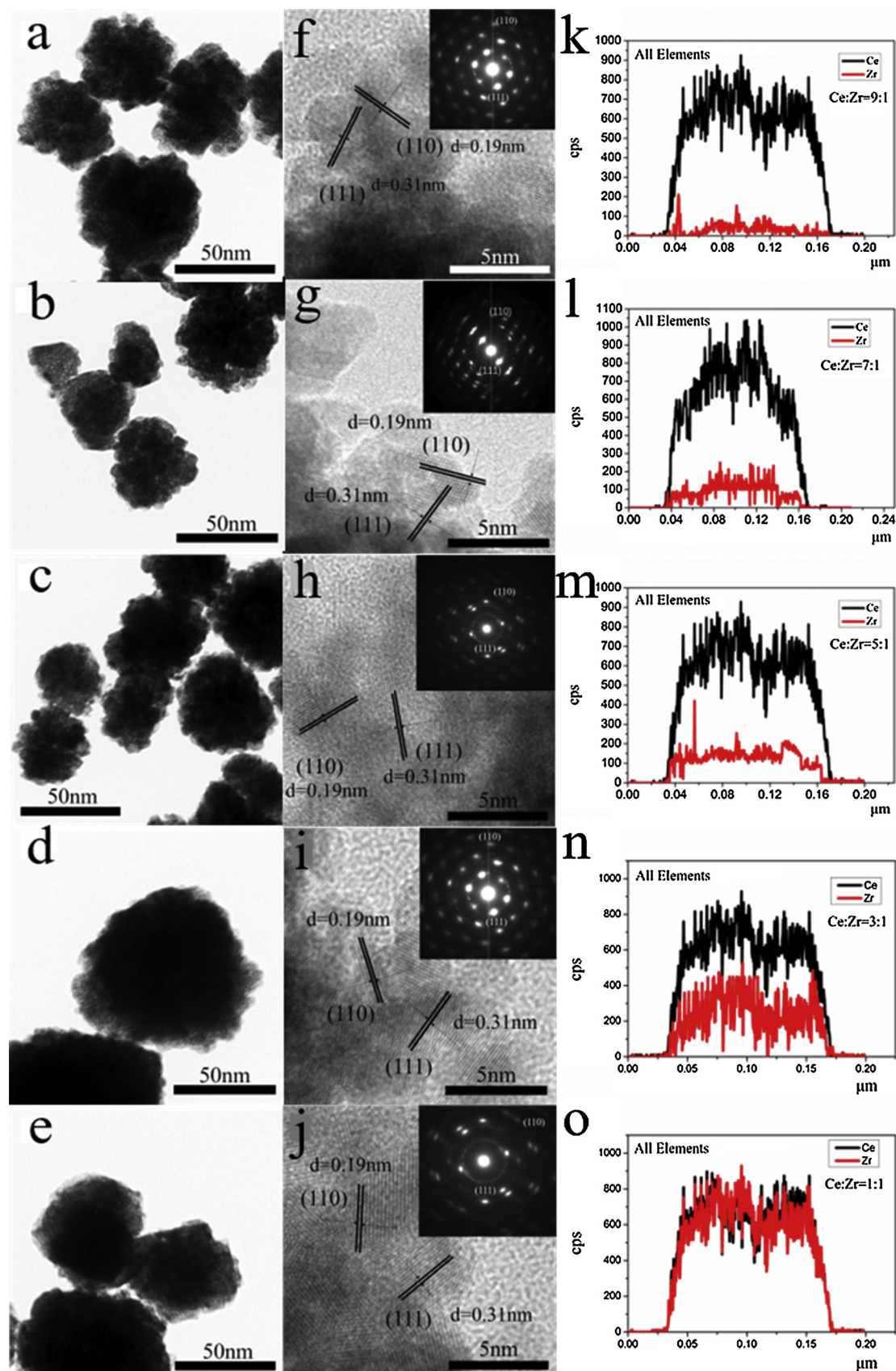


**Fig. 2.** (a–e) TEM images and (f–j) HRTEM images and (k–o) EDS scans of  $\text{Ce}_x\text{Zr}_y\text{O}_2$  nanocomposites with the Ce:Zr molar ratios varied from 9:1 to 1:1. The corresponding SAED patterns are depicted in the insets to the respective HRTEM images in (f–j).

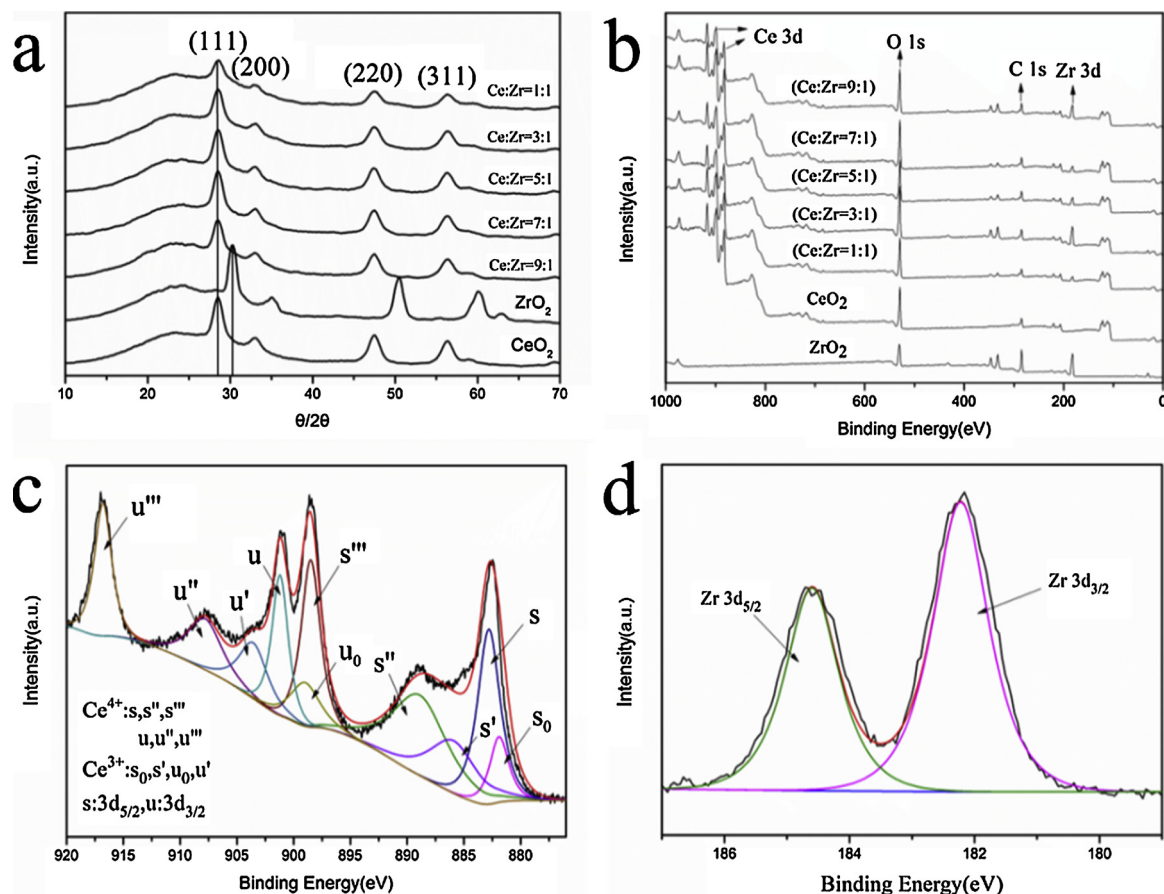


**Fig. 3.** (a) XRD patterns of  $\text{CeO}_2$ ,  $\text{ZrO}_2$  and  $\text{Ce}_x\text{Zr}_y\text{O}_2$  nanocomposites. (b) XPS spectra of  $\text{Ce}_x\text{Zr}_y\text{O}_2$  nanocomposites,  $\text{CeO}_2$  and  $\text{ZrO}_2$ . High-resolution XPS spectra of the (c) Ce and (d) Zr region of the  $\text{Ce}_x\text{Zr}_y\text{O}_2$  nanocomposites.

in solution. In Fig. 2f-j, one can see that all  $\text{Ce}_x\text{Zr}_y\text{O}_2$  samples exhibit clearly defined (110) and (111) crystalline facets with interplanar spacings of 0.19 nm and 0.31 nm, respectively. Furthermore, EDS measurements in Fig. 2k-o show that the elemental percentage of Zr increased from 10% to 50% while the elemental percentage of Ce decreased from 90% to 50%.

The phase structures of the  $\text{Ce}_x\text{Zr}_y\text{O}_2$  nanocomposites were then characterized by XRD measurements. Fig. 3a depicts the XRD patterns of  $\text{CeO}_2$ ,  $\text{ZrO}_2$ , and  $\text{Ce}_x\text{Zr}_y\text{O}_2$  prepared at different Ce:Zr molar ratios. A series of well-defined diffraction peaks can be identified at  $28.6^\circ$ ,  $33.2^\circ$ ,  $47.6^\circ$ , and  $56.4^\circ$ , corresponding to the (111), (200), (220), and (311) diffractions of  $\text{CeO}_2$ , consistent with a typical cubic fluorite structure (JCPDS card no. 34-0394) [35,36]. From Fig. 3a, it can be seen that there is no obvious  $\text{ZrO}_x$  diffraction peak, which might be due to the low crystallinity of  $\text{ZrO}_x$  [31,35]. At increasing Zr loading, one can observe that the (111) peak became gradually broadened and the full width at half-maximum increased from 0.950 at Ce:Zr = 9:1 to 1.013 at Ce:Zr = 1:1. The incorporation of  $\text{ZrO}_2$  into  $\text{CeO}_2$  lattices and the formation of a solid solution led to shrinkage of the lattices due to the replacement of cerium with smaller zirconium [31,37].

Further investigations of the  $\text{Ce}_x\text{Zr}_y\text{O}_2$  nanocomposites were conducted by XPS analysis. Fig. 3b shows the XPS spectra of the series. From Fig. 3c, the  $s_0$ ,  $s$ ,  $s'$ ,  $s''$ , and  $s'''$  peaks were attributed to the  $\text{Ce} 3d_{5/2}$  electrons, and  $u_0$ ,  $u$ ,  $u'$ ,  $u''$ , and  $u'''$  to the  $\text{Ce} 3d_{3/2}$  electrons. Of these, the  $s$ ,  $s''$ ,  $s'''$ ,  $u$ ,  $u''$ , and  $u'''$  peaks were due to  $\text{Ce}^{4+}$ , and the  $s_0$ ,  $s'$ ,  $u_0$ , and  $u'$  ones to  $\text{Ce}^{3+}$  [38–40]. Based on the integrated peak areas, it can be found that  $\text{Ce}^{3+}$  and  $\text{Ce}^{4+}$  accounted for 4/7 and 3/7 of the total Ce concentration, respectively. The  $\text{Zr} 3d_{5/2}$  and  $\text{Zr} 3d_{3/2}$  electrons can be identified at 184.8 eV and 182.2 eV (Fig. 3d), indicating that zirconium was mostly in the  $\text{Zr}^{4+}$  valence state [41,42].

Transient photocurrent analysis was an effective method to evaluate the separation efficiency of photogenerated electrons and holes. As shown in Fig. 4a, rapid and stable photocurrent responses were produced for all samples under four intermittent on-off cycles of photo-irradiation at  $\lambda > 420$  nm. Among the series, the  $\text{Ce}_{0.9}\text{Zr}_{0.1}\text{O}_2$  sample exhibited the highest photocurrent, suggesting the best efficiency in the separation of photogenerated electron-hole pairs under visible light irradiation [43].

EIS is another effective method to examine the efficient separation of photogenerated charges [23]. As can be seen from Fig. 4b, the  $\text{Ce}_{0.9}\text{Zr}_{0.1}\text{O}_2$  sample showed the smallest diameter of the semicircle, indicating that the charge-transfer resistance ( $R_{ct}$ ) was the lowest among the series of catalysts. It can be seen from Fig. 4c that the internal resistance ( $R_s$ ) of all catalysts was very close, wherein the  $\text{Ce}_{0.9}\text{Zr}_{0.1}\text{O}_2$  sample showed a slightly smaller  $R_s$  than others [43]. This suggests a somewhat enhanced efficiency in the separation of electrons and holes, due to faster electron transition from the valence band to the conduction band, in good agreement with the photocurrent results in Fig. 4a.

To clarify the energy band structure and interfacial charge transfer, UV-vis diffuse reflectance spectroscopic (DRS) analysis was conducted and the results were presented in Fig. 4d. It can be seen that all catalysts showed a rather well-defined photo absorption edge at approximately 550 nm for the  $\text{Ce}_{0.9}\text{Zr}_{0.1}\text{O}_2$  sample and between 350–400 nm for the others. With the addition of a small amount of Zr, the absorbance of the catalysts was significantly enhanced. However, as the Zr content continued to increase, the absorption edge of the catalyst blue-shifted. This indicates that the addition of Zr played an important role in regulating light absorption of the catalyst. In addition, from the Tauc plots in the inset to Fig. 4d, the band gap energy of the catalysts can be estimated

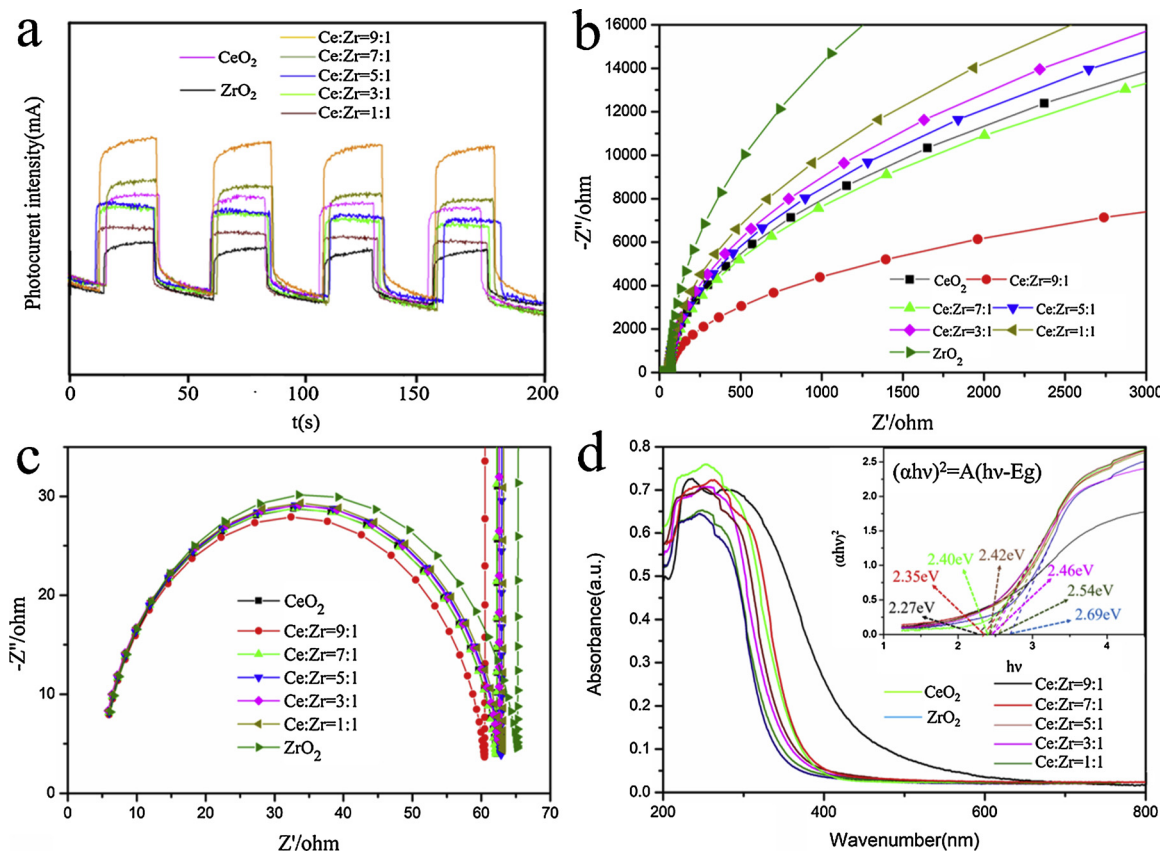


**Fig. 4.** (a) Photocurrent response of the Ce<sub>x</sub>Zr<sub>y</sub>O<sub>2</sub> nanocomposites, CeO<sub>2</sub> and ZrO<sub>2</sub> under visible light irradiation ( $\lambda > 420$  nm). (b) and (c) Nyquist plots of the various Ce<sub>x</sub>Zr<sub>y</sub>O<sub>2</sub> nanocomposites, CeO<sub>2</sub> and ZrO<sub>2</sub>. (d) UV-vis diffuse reflectance spectra and  $(\alpha h\nu)^2$  versus  $h\nu$  curves for the various Ce<sub>x</sub>Zr<sub>y</sub>O<sub>2</sub> nanocomposites, CeO<sub>2</sub> and ZrO<sub>2</sub>.

by extrapolating the tangent to the  $x$ -axis, which was 2.40 eV for CeO<sub>2</sub>, 2.27 eV for Ce:Zr = 9:1, 2.35 eV for Ce:Zr = 7:1, 2.42 eV for Ce:Zr = 5:1, 2.46 eV for Ce:Zr = 3:1, 2.54 eV for Ce:Zr = 1:1, and 2.69 eV for ZrO<sub>2</sub>. That was, the Ce<sub>0.9</sub>Zr<sub>0.1</sub>O<sub>2</sub> sample exhibited the lowest band gap among the series [23,44]. A smaller band gap energy generally corresponds to a more efficient electron transition from the valence band to the conduction band. Consistent results were obtained from DFT calculations, where the band gap energies were estimated to be 2.171 eV for CeO<sub>2</sub>, 1.882 eV for Ce:Zr = 9:1, 2.068 eV for Ce:Zr = 7:1, 2.236 eV for Ce:Zr = 5:1, 2.259 eV for Ce:Zr = 3:1, 2.461 eV for Ce:Zr = 1:1, and 4.619 eV for ZrO<sub>2</sub>. The Ce:Zr = 9:1 sample stood out with the lowest band gap, consistent with the experimental results.

As is well known, free radicals such as  $\cdot\text{O}_2^-$  and  $\cdot\text{OH}$  are the active species responsible for the photocatalytic degradation of organic pollutants in wastewater [23]. ESR measurements were then conducted to analyze the generation of  $\cdot\text{O}_2^-$  and  $\cdot\text{OH}$  radicals by the nanocomposite catalysts.  $\cdot\text{O}_2^-$  reacts with water easily, but does not react with methanol, and  $\cdot\text{O}_2^-$  has a longer half-life in methanol, so the signal of  $\cdot\text{O}_2^-$  can be captured by DMPO in methanol. As  $\cdot\text{OH}$  reacts readily with alcohol, the signal of  $\cdot\text{OH}$  can be captured in water. From Fig. 5, no ESR signal was observed in the dark with the samples at Ce:Zr = 9:1, 7:1, and 1:1. After visible light photoirradiation ( $\lambda > 400$  nm), the signals of DMPO- $\cdot\text{O}_2^-$  and DMPO- $\cdot\text{OH}$  became well-defined in all three catalysts, and were the strongest with the 9:1 sample. This suggests that the Ce<sub>0.9</sub>Zr<sub>0.1</sub>O<sub>2</sub> sample is the optimal catalyst for the photocatalytic degradation of sulfonamides among the series [16,23,45].

### 3.2. Photocatalytic performance

The degradation efficiency of sulfonamides by Ce<sub>x</sub>Zr<sub>y</sub>O<sub>2</sub> nanocomposites was evaluated by UV-vis diffuse reflectance spectroscopy.

The nanocomposites were dispersed in a sulfonamide solution. Before photoirradiation, the dispersion was allowed for adsorption-desorption equilibrium in the dark for 60 min. Fig. 6a showed the variation of C/C<sub>0</sub> with photoirradiation time for the Ce<sub>x</sub>Zr<sub>y</sub>O<sub>2</sub> nanocomposite samples, where C<sub>0</sub> and C were the sulfonamide concentration before and after photoirradiation, respectively [46]. It can be found that the Ce:Zr molar ratio in the preparation of the nanocomposites played an important role in controlling the photocatalytic performance. From Fig. 6a, one could see that the photocatalytic performance of the Ce<sub>x</sub>Zr<sub>y</sub>O<sub>2</sub> nanocomposites decreased as the content of Zr increased.

It can be seen from Fig. 6a that in the absence of catalysts, there was virtually no degradation of sulfonamide under visible light illumination. In fact, even after photoirradiation for 30 min, the sulfonamide concentration decreased by only 1.8%. In the presence of Ce<sub>x</sub>Zr<sub>y</sub>O<sub>2</sub> nanocomposites, the photocatalytic degradation rates were markedly enhanced, 84.38% for CeO<sub>2</sub>, 91.33% for Ce:Zr = 9:1, 86.93% for Ce:Zr = 7:1, 69% for Ce:Zr = 5:1, 64.37% for Ce:Zr = 3:1, 62.84% for Ce:Zr = 1:1, and 51.17% for ZrO<sub>2</sub>. Obviously, the Ce<sub>0.9</sub>Zr<sub>0.1</sub>O<sub>2</sub> sample exhibited the best photocatalytic performance within the present experimental context [47]. This coincides with the largest specific surface area determined by nitrogen adsorption/desorption analysis (Fig. S1).

Fig. 6b depicts the photocatalytic degradation of sulfonamide at different pH, where the degradation rate can be seen to reach the maximum at neutral pH condition. In the acidic solution, protons consumed  $\cdot\text{O}_2^-$ , thereby reducing the degradation of sulfonamide. In alkaline solutions (pH = 10), electrostatic repulsion between the negatively charged sulfonamide and negatively charged surface of Ce<sub>x</sub>Zr<sub>y</sub>O<sub>2</sub> hindered their contact, leading to a drop in the photodegradation rate [23].

The loading of the nanocomposites was also found to impact the degradation rate of sulfonamide. At the sulfonamide concentration of

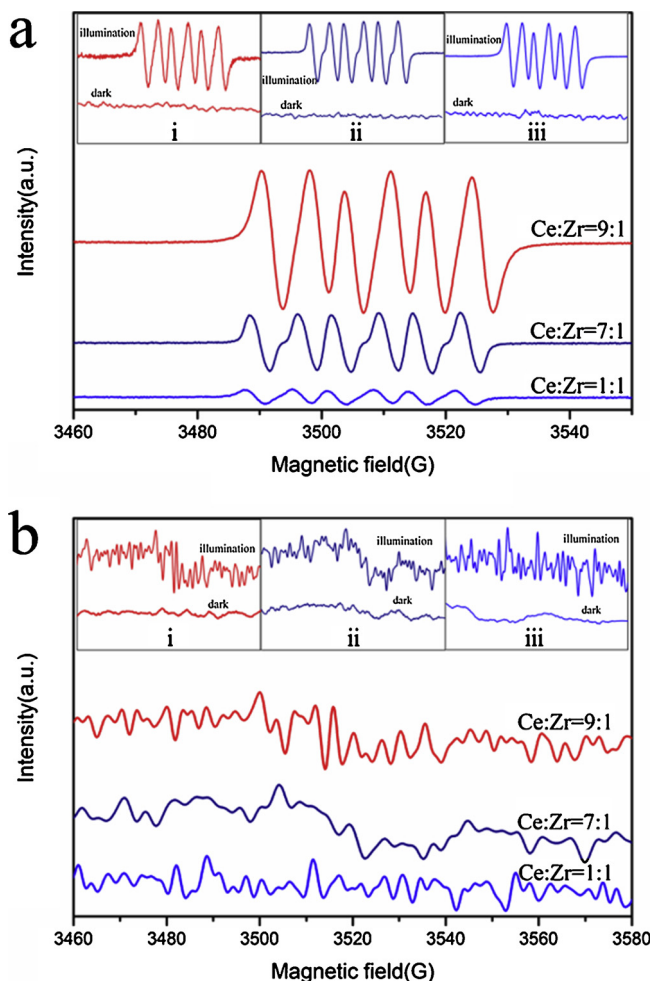


**Fig. 5.** (a) ESR spectra of DMPO-·O<sub>2</sub><sup>-</sup> and (b) DMPO-·OH adducted over the various Ce<sub>x</sub>Zr<sub>y</sub>O<sub>2</sub> nanocomposites after visible light irradiation for 5 min. The insets are a comparison of DMPO-·O<sub>2</sub><sup>-</sup> and DMPO-·OH from each catalyst under light and dark conditions.

0.01 g L<sup>-1</sup>, four sets of experiments were conducted for comparison. Fig. 6c shows the degradation of sulfonamide during 30 min of photo illumination in the presence of the Ce<sub>0.9</sub>Zr<sub>0.1</sub>O<sub>2</sub> sample at different loadings. It can be seen that as the amount of the added catalyst increased, the degradation of sulfonamide was initially improved, but diminished with a further increase of the catalyst loading, with the optimal loading of 0.1 g L<sup>-1</sup>. This was likely due to reduced light permeation by the excessive amount of the catalyst [16].

In order to study the role of free radicals in photocatalytic process, isopropanol (IPA), ethylenediamine tetraacetic acid disodium salt (EDTA-2Na) and benzoquinone (BQ) were added to the solution as they are well-known scavengers for ·OH, h<sup>+</sup>, and ·O<sub>2</sub><sup>-</sup>. From Fig. 7a, it can be seen that after 30 min of visible light irradiation, the addition of IPA and BQ significantly inhibited sulfonamide degradation, while no apparent impact was observed with EDTA-2Na. This indicates that under visible light irradiation, Ce<sub>0.9</sub>Zr<sub>0.1</sub>O<sub>2</sub> primarily produced ·OH, h<sup>+</sup>, and ·O<sub>2</sub><sup>-</sup> free radicals for the photocatalytic degradation of sulfonamide, while h<sup>+</sup> played a minor role. Among them, ·OH was the most important active substance involved in the reaction [16].

The corresponding apparent quantum efficiency (AQE) at various wavelengths was shown in Fig. 7b, which decreased with increasing incident light wavelength, and exhibited a variation trend consistent with the optical absorption profile. This suggests that the degradation of sulfonamide was indeed driven by light-induced carriers [48–50]. This can also be manifested in the action spectrum of the photocatalytic

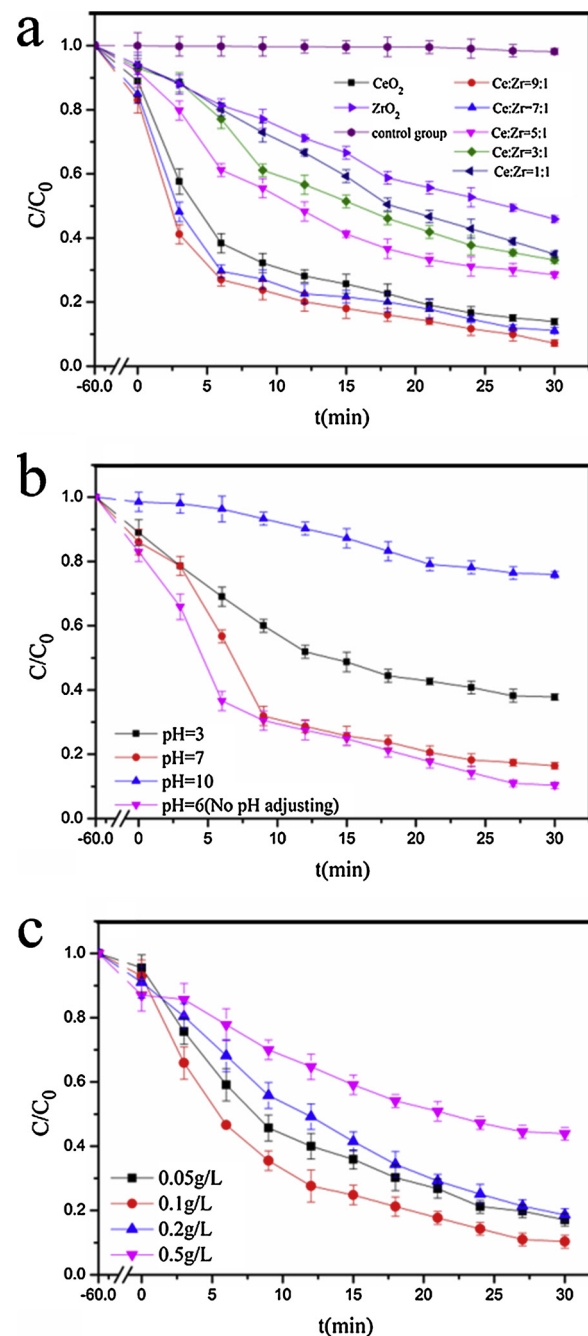


**Fig. 6.** (a) Photocatalytic degradation of sulfonamide by CeO<sub>2</sub>, ZrO<sub>2</sub> and Ce<sub>x</sub>Zr<sub>y</sub>O<sub>2</sub> nanocomposites. (b) Photocatalytic degradation of sulfonamide at pH = 3, 6, 7, and 10. Catalyst concentration 0.1 g L<sup>-1</sup>, and sulfonamide concentration 0.01 g L<sup>-1</sup>. (c) Degradation of sulfonamide under visible light at different catalyst loadings at pH = 6.5. Sulfonamide concentration 0.01 g L<sup>-1</sup>.

test in the upper right inset to Fig. 7b.

In order to study the stability of the Ce<sub>x</sub>Zr<sub>y</sub>O<sub>2</sub> samples, the Ce<sub>0.9</sub>Zr<sub>0.1</sub>O<sub>2</sub> nanocomposite was examined by XRD measurements before and after the photocatalytic tests. From Fig. 7c, one can see that the diffraction patterns remained well-defined and virtually unchanged, indicating high structural integrity of the sample [51]. The nanocomposite stability was further tested by comparing the photocatalytic performance after repeated uses. From Fig. 7d, the Ce<sub>0.9</sub>Zr<sub>0.1</sub>O<sub>2</sub> sample can be seen to exhibit only less than 5% change of the activity after 5 repeated uses. Taken together, these results showed high structural stability of the Ce<sub>x</sub>Zr<sub>y</sub>O<sub>2</sub> nanocomposite in the photocatalytic degradation of sulfonamide [50].

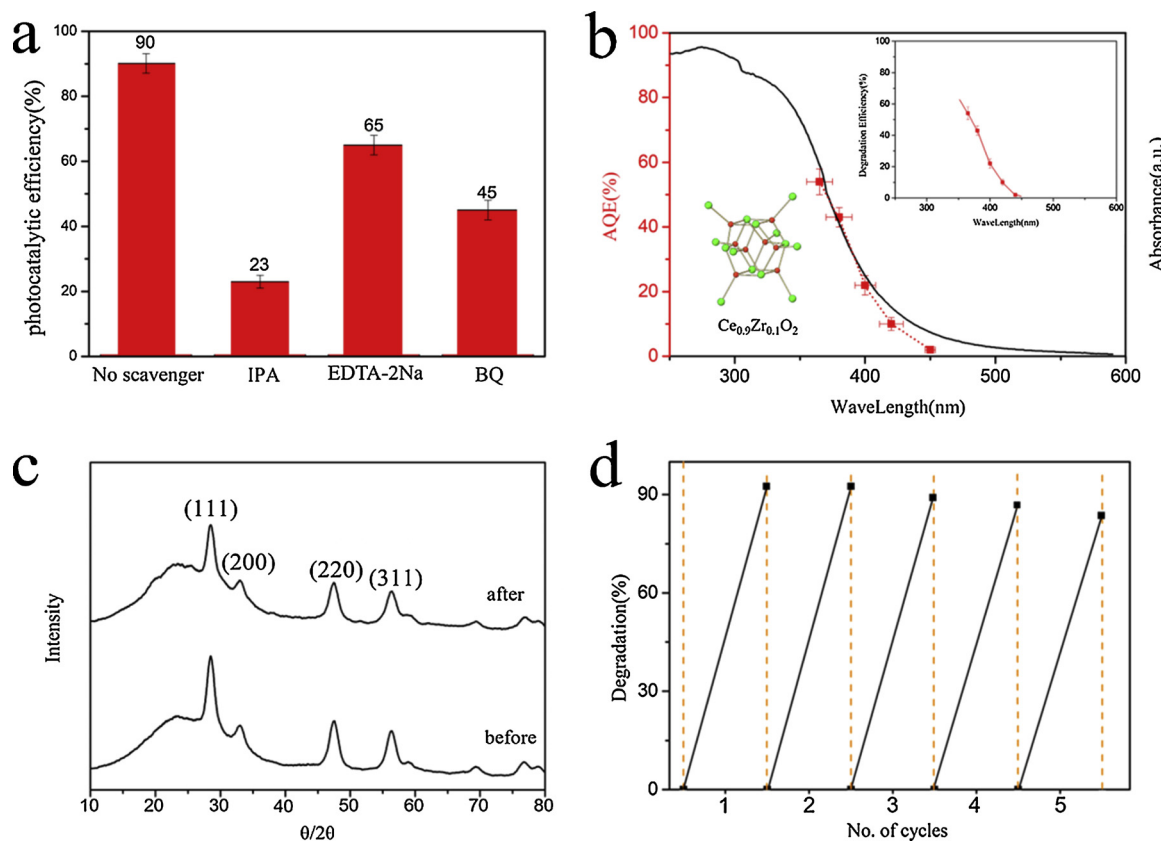


**Fig. 7.** (a) Comparison of photocatalytic degradation of sulfonamide in the absence and presence of various radical scavengers at pH = 6.5 after visible light photoirradiation for 30 min. (b) Apparent quantum efficiency (AQE, left y axis) of sulfonamide photodegradation by Ce<sub>0.9</sub>Zr<sub>0.1</sub>O<sub>2</sub> at different wavelengths, along with the absorption spectrum (right y axis). The insets in the upper right corner is the action spectrum of the photocatalytic test, the insets in the lower left corner is a three-dimensional model of molecular structure of Ce<sub>0.9</sub>Zr<sub>0.1</sub>O<sub>2</sub>. (c) XRD diffraction patterns of Ce<sub>0.9</sub>Zr<sub>0.1</sub>O<sub>2</sub> before and after photocatalytic degradation of sulfonamide. (d) Repeated photocatalytic tests of Ce<sub>0.9</sub>Zr<sub>0.1</sub>O<sub>2</sub>.

The impacts of ·OH radicals on the photodegradation efficiency are further examined by fluorescence measurements (at 315 nm excitation). Fig. 8 depicts the corresponding emission spectra in the (a) presence and (b) absence of the Ce<sub>0.9</sub>Zr<sub>0.1</sub>O<sub>2</sub> nanocomposite under UV photo-irradiation, in comparison to those acquired in the dark but in the presence of the catalyst (Fig. 8c). Samples were taken every 5 min for fluorescence analysis. From Fig. 8a, an emission peak can be seen to emerge at 425 nm and the intensity increases markedly with prolonging irradiation time, which indicates that the formation of ·OH radicals was favored under photoirradiation. For comparison, the fluorescence emission intensity was markedly reduced without the nanocomposite (Fig. 8b), and no obvious fluorescence emission was seen in the dark even in the presence of the catalyst (Fig. 8c). This indicates that the production of ·OH radicals can be significantly enhanced upon the addition of the Ce<sub>0.9</sub>Zr<sub>0.1</sub>O<sub>2</sub> nanocomposite. In fact, as illustrated in Fig. 8d, the concentration of ·OH radicals produced increased linearly with the reaction time [51].

### 3.3. Degradation pathway

Mass spectrometric measurements were then carried out to evaluate the reaction intermediates and pathway of sulfonamide photodegradation. A series of peaks were detected within the *m/z* range of 210 to 110. The peak at *m/z* 174.02 (C<sub>1</sub>, MW 174.02, Fig. S2) can be ascribed to protonated sulfonamide (MW 173.04, Fig. S3), or to the substitution of the amino group (-NH<sub>2</sub>) by hydroxyl (-OH) as a result of the ·OH attack (C<sub>2</sub>, MW 174.02, Fig. S4). The peak at *m/z* 110.06 is likely due to -OH attack of the C-S bond to further hydroxylate the reactant (C<sub>3</sub>, MW 110.06, Fig. S5). The -NH<sub>2</sub> in the C<sub>3</sub> and -OH in the

para position were further oxidized to form the nitro group (-NO<sub>2</sub>) (C<sub>4</sub>, MW 138.02, Fig. S6). The peak at 201.00 arose from oxidation of the -NH<sub>2</sub> group attached to the benzene ring in sulfonamide to form a nitro group (-NO<sub>2</sub>) (C<sub>5</sub>, MW 201.00, Fig. S7), where the -OH group attacked the S-N bond to form a sulfonic acid group (C<sub>6</sub>, MW 201.98, Fig. S8), and the hydroxyl group (-OH) further replaced the sulfonic acid group to form C<sub>4</sub> (MW 138.02, Fig. S6). The peak at 189.03 was detected by combining a hydroxyl group (-OH) above the benzene ring to form C<sub>7</sub> (MW 189.03, Fig. S9), which was detected by both the positive and negative modes of mass spectrometry. The C<sub>8</sub> peak (MW 188.00, Fig. S10) had a dominant response in positive-mode mass spectrometry, and thus was most likely a sulfonic acid-based hydroxyl group forming an intramolecular hydrogen bond. By contrast, the C<sub>9</sub> peak (MW 190.02, Fig. S11) had a dominant response in negative-mode mass spectrometry, most likely due to an amino-terminated hydroxyl group which formed an intramolecular hydrogen bond. Finally, the benzene ring was opened by radical attack, and all the organic intermediates were further mineralized to CO<sub>2</sub>, H<sub>2</sub>O and mineral acids under visible photo-irradiation. On the basis of the detected reaction intermediates, a degradation pathway of sulfonamide was proposed in Fig. 9 which involves four major steps: (1) hydroxylation; (2) breaking of S-N bond; (3) breaking of C-N bond; (4) oxidation and mineralization of organic intermediates [16,52–56].

### 3.4. Mechanism for sulfonamide photodegradation

The results presented above show that Ce<sub>x</sub>Zr<sub>y</sub>O<sub>2</sub> nanocomposites possessed apparent photocatalytic activity in degrading sulfonamide under visible light irradiation, because (i) the incorporation of Zr into

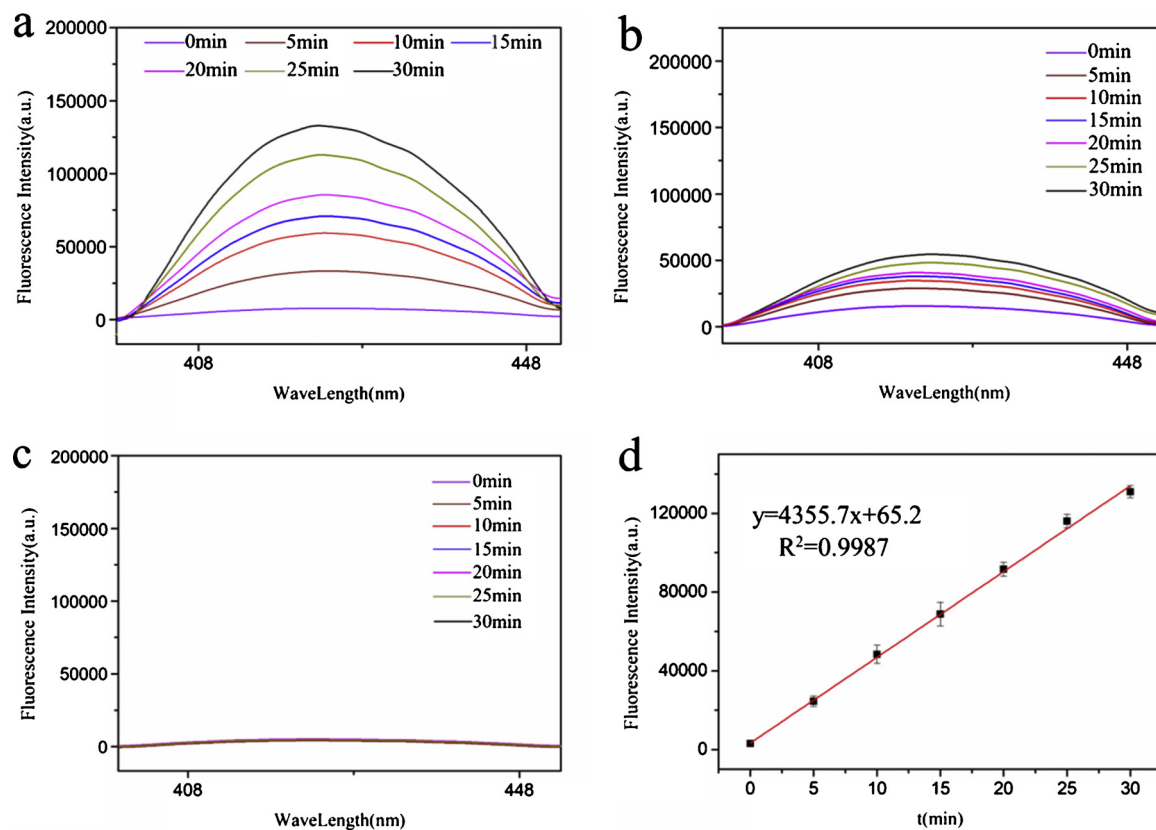


**Fig. 8.** Fluorescence emission spectra of sulfonamide degradation in the (a) presence and (b) absence of  $\text{Ce}_{0.9}\text{Zr}_{0.1}\text{O}_2$  under 315 nm excitation. Catalyst concentration  $0.1 \text{ g L}^{-1}$  and solution pH 6. (b) Fluorescence emission spectra acquired in the presence of  $\text{Ce}_{0.9}\text{Zr}_{0.1}\text{O}_2$  but acquired in the dark. (d) Variation of fluorescence intensity with light irradiation time in the presence of  $\text{Ce}_{0.9}\text{Zr}_{0.1}\text{O}_2$ . Symbols are data obtained from panel (a) and line is linear regression.

$\text{CeO}_2$  led to narrowing of the metal oxide band gap which extended the light absorption to the visible range, as manifested in UV-vis DRS spectroscopic measurements; and (ii) the specific surface area of  $\text{Ce}_x\text{Zr}_y\text{O}_2$  nanocomposites increased markedly (Fig. S1), as compared to

that of  $\text{CeO}_2$ , which facilitated the access to adsorption sites as well as catalytic sites during the photocatalytic reaction [16].

The possible mechanism of sulfonamide degradation by  $\text{Ce}_x\text{Zr}_y\text{O}_2$  nanocomposites was illustrated in Fig. 10. Under visible light

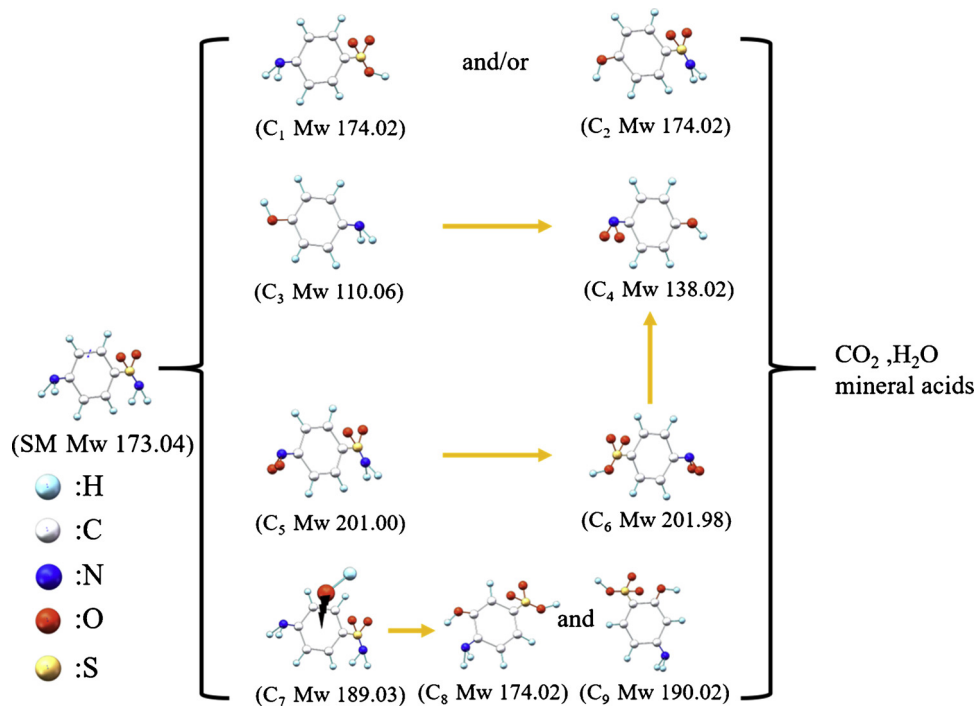


**Fig. 9.** Proposed reaction pathway for photocatalytic degradation of sulfonamide by  $\text{Ce}_x\text{Zr}_y\text{O}_2$  nanocomposites.

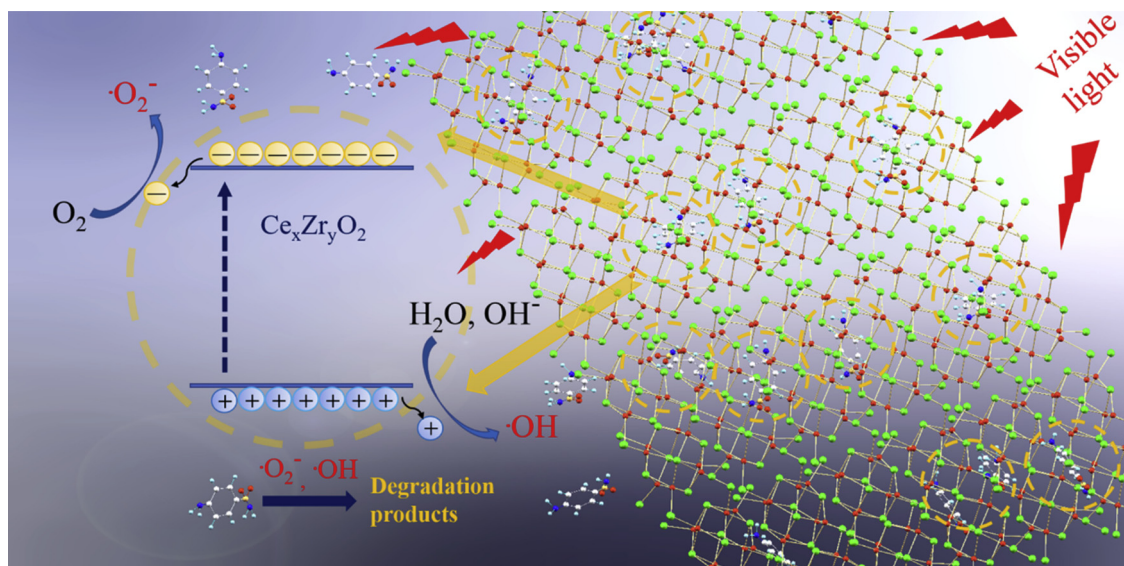


**Fig. 10.** Schematic illustration of the proposed mechanism for the degradation of sulfonamide by  $\text{Ce}_x\text{Zr}_y\text{O}_2$  nanocomposites under visible light irradiation.

photoirradiation,  $\text{Ce}_x\text{Zr}_y\text{O}_2$  absorbs photons generating electron-hole pairs. The photogenerated electrons are then scavenged by dissolved oxygen ( $\text{O}_2$ ) in water, resulting in effective electron-hole separation and production of  $\cdot\text{O}_2^-$  radicals. These  $\cdot\text{O}_2^-$  radicals can be converted to  $\text{HOO}'$ , and combine with trapped electrons to generate  $\text{H}_2\text{O}_2$ , leading to the generation of  $\cdot\text{OH}$  radicals. Concurrently, the holes left on the valence band of the  $\text{Ce}_x\text{Zr}_y\text{O}_2$  nanocomposites react with water and/or surface hydroxyl ( $\text{-OH}$ ) to form hydroxyl radicals ( $\cdot\text{OH}$ ). These radicals attack sulfonamide in the close vicinity, resulting in the degradation and mineralization of sulfonamide [16,23,45,57–60].

#### 4. Conclusion

A series of  $\text{Ce}_x\text{Zr}_y\text{O}_2$  nanocomposites were successfully synthesized through a convenient hydrothermal method with the Ce:Zr molar feed ratio varied from 9:1 to 1:1. Whereas the morphological characteristics of the resulting nanocomposites did not vary significantly, the  $\text{Ce}_{0.9}\text{Zr}_{0.1}\text{O}_2$  sample was found to exhibit the largest specific surface area, smallest bandgap, highest photocurrents, and lowest impedance among the series. The photocatalytic activity towards the photo-degradation of sulfonamide was then evaluated and compared, and the  $\text{Ce}_{0.9}\text{Zr}_{0.1}\text{O}_2$  sample was found to demonstrate the best performance with a degradation rate of 91.33% for sulfonamide under visible light illumination for 30 min, where photogenerated  $\cdot\text{OH}$  radicals were found to play a dominant role. On the basis of the result obtained from mass spectrometric measurements of the reaction intermediates, a reaction pathway and mechanism were proposed to account for sulfonamide degradation. In all, the results from this study suggest that  $\text{Ce}_x\text{Zr}_y\text{O}_2$  nanocomposites can be exploited as effective catalysts for the photodegradation of sulfonamide antibiotics.

#### Declaration of Competing Interest

The authors declare that they have no known competing financial interests or personal relationships that could have appeared to influence the work reported in this paper.

#### Acknowledgments

This work was supported by the National Science Foundation (CBET-1848841) and the Natural Science Foundation of China (NSFC, No. 21471103, 51631001), the Scientific Research Base Development Program and the science and technology innovation service ability

construction project of the Beijing Municipal Commission of Education.

#### Appendix A. Supplementary data

Supplementary material related to this article can be found, in the online version, at doi:<https://doi.org/10.1016/j.apcatb.2019.118107>.

#### References

- [1] J. Peng, E. Wu, N. Wang, X. Quan, M. Sun, Q. Hu, Removal of sulfonamide antibiotics from water by adsorption and persulfate oxidation process, *J. Mol. Liq.* 274 (2019) 632–638.
- [2] Z. Chen, X. Xiao, B. Xing, B. Chen, pH-dependent sorption of sulfonamide antibiotics onto biochar: sorption mechanisms and modeling, *Environ. Pollut.* 248 (2019) 48–56.
- [3] L. Ma, C. Yang, X. Tian, Y. Nie, Z. Zhou, Y. Li, Enhanced usage of visible light by BiSex for photocatalytic degradation of methylene blue in water via the tunable band gap and energy band position, *J. Clean. Prod.* 171 (2018) 538–547.
- [4] M.B. Ahmed, J.L. Zhou, H.H. Ngo, W. Guo, M.A.H. Johir, K. Sornalingam, Single and competitive sorption properties and mechanism of functionalized biochar for removing sulfonamide antibiotics from water, *Chem. Eng. J.* 311 (2017) 348–358.
- [5] M. Sarker, B.N. Bhadra, P.W. Seo, S.H. Jhung, Adsorption of benzotriazole and benzimidazole from water over a Co-based metal azolate framework MAF-5(Co), *J. Hazard. Mater.* 324 (2017) 131–138.
- [6] G. Zhao, C. Li, X. Wu, J. Yu, X. Jiang, W. Hu, F. Jiao, Reduced graphene oxide modified NiFe-calcinated layered double hydroxides for enhanced photocatalytic removal of methylene blue, *Appl. Surf. Sci.* 434 (2018) 251–259.
- [7] L. Chen, J. He, Y. Liu, P. Chen, C.-T. Au, S.-F. Yin, Recent advances in bismuth-containing photocatalysts with heterojunctions, *Chin. J. Catal.* 37 (2016) 780–791.
- [8] M. Cheng, G. Zeng, D. Huang, C. Lai, P. Xu, C. Zhang, Y. Liu, Hydroxyl radicals based advanced oxidation processes (AOPs) for remediation of soils contaminated with organic compounds: a review, *Chem. Eng. J.* 284 (2016) 582–598.
- [9] M. Ge, C. Cao, J. Huang, S. Li, Z. Chen, K.-Q. Zhang, S.S. Al-Deyab, Y. Lai, A review of one-dimensional  $\text{TiO}_2$  nanostructured materials for environmental and energy applications, *J. Mater. Chem. A* 4 (2016) 6772–6801.
- [10] C. Liu, D. Kong, P.C. Hsu, H. Yuan, H.W. Lee, Y. Liu, H. Wang, S. Wang, K. Yan, D. Lin, P.A. Maraccini, K.M. Parker, A.B. Boehm, Y. Cui, Rapid water disinfection using vertically aligned  $\text{MoS}_2$  nanofilms and visible light, *Nat. Nanotechnol.* 11 (2016) 1098–1104.
- [11] M.A. Shannon, P.W. Bohn, M. Elimelech, J.G. Georgiadis, B.J. Marinas, A.M. Mayes, Science and technology for water purification in the coming decades, *Nature* 452 (2008) 301–310.
- [12] M.F. Abdel Messih, M.A. Ahmed, A. Soltan, S.S. Anis, Facile approach for homogeneous dispersion of metallic silver nanoparticles on the surface of mesoporous titania for photocatalytic degradation of methylene blue and indigo carmine dyes, *J. Photochem. Photobiol. A* 335 (2017) 40–51.
- [13] L. Wang, Y. Wu, Y. Zheng, L. Liu, F. Zhao, Efficient degradation of sulfamethoxazole and the response of microbial communities in microbial fuel cells, *RSC Adv.* 5 (2015) 56430–56437.
- [14] M.R. Hoffmann, S.T. Martin, W. Choi, D.W. Bahnemann, Environmental applications of semiconductor photocatalysis, *Chem. Rev.* 95 (1995) 69–96.
- [15] M. Dlugosz, P. Zmudzki, A. Kwiecien, K. Szczubialka, J. Krzek, M. Nowakowska, Photocatalytic degradation of sulfamethoxazole in aqueous solution using a floating

TiO<sub>2</sub>-expanded perlite photocatalyst, *J. Hazard. Mater.* 298 (2015) 146–153.

[16] W. Zhu, F. Sun, R. Goei, Y. Zhou, Facile fabrication of RGO-WO<sub>3</sub> composites for effective visible light photocatalytic degradation of sulfamethoxazole, *Appl. Catal. B* 207 (2017) 93–102.

[17] V. Augugliaro, M. Bellardita, V. Loddo, G. Palmisano, L. Palmisano, S. Yurdakal, Overview on oxidation mechanisms of organic compounds by TiO<sub>2</sub> in heterogeneous photocatalysis, *J. Photochem. Photobiol. C* 13 (2012) 224–245.

[18] M.N. Chong, B. Jin, C.W. Chow, C. Saint, Recent developments in photocatalytic water treatment technology: a review, *Water Res.* 44 (2010) 2997–3027.

[19] L. Huang, M. He, B. Chen, B. Hu, A designable magnetic MOF composite and facile coordination-based post-synthetic strategy for the enhanced removal of Hg<sup>2+</sup> from water, *J. Mater. Chem. A* 3 (2015) 11587–11595.

[20] J.A. Park, B. Yang, J. Lee, I.G. Kim, J.H. Kim, J.W. Choi, H.D. Park, I.W. Nah, S.H. Lee, Ultrasonic spray pyrolysis synthesis of reduced graphene oxide/anatase TiO<sub>2</sub> composite and its application in the photocatalytic degradation of methylene blue in water, *Chemosphere* 191 (2018) 738–746.

[21] K.-S. Kim, S.K. Kam, Y.S. Mok, Elucidation of the degradation pathways of sulfonamide antibiotics in a dielectric barrier discharge plasma system, *Chem. Eng. J.* 271 (2015) 31–42.

[22] Y. Song, J. Tian, S. Gao, P. Shao, J. Qi, F. Cui, Photodegradation of sulfonamides by g-C<sub>3</sub>N<sub>4</sub> under visible light irradiation: effectiveness, mechanism and pathways, *Appl. Catal. B* 210 (2017) 88–96.

[23] G. Di, Z. Zhu, H. Zhang, J. Zhu, Y. Qiu, D. Yin, S. Kuppers, Visible-light degradation of sulfonamides by Z-schema ZnO/g-C<sub>3</sub>N<sub>4</sub> heterojunctions with amorphous Fe<sub>2</sub>O<sub>3</sub> as electron mediator, *J. Colloid Interface Sci.* 538 (2019) 256–266.

[24] P. Latha, K. Prakash, S. Karuthapandian, Enhanced visible light photocatalytic activity of CeO<sub>2</sub>/alumina nanocomposite: synthesized via facile mixing-calcination method for dye degradation, *Adv. Powder Technol.* 28 (2017) 2903–2913.

[25] Y. Hao, L. Li, J. Zhang, H. Luo, X. Zhang, E. Chen, Multilayer and open structure of dendritic crosslinked CeO<sub>2</sub>-ZrO<sub>2</sub> composite: enhanced photocatalytic degradation and water splitting performance, *Int. J. Hydrogen Energy* 42 (2017) 5916–5929.

[26] N.A. Abdelwhab, E.M.H. Morsy, Synthesis and characterization of methyl pyrazolone functionalized magnetic chitosan composite for visible light photocatalytic degradation of methylene blue, *Int. J. Biol. Macromol.* 108 (2018) 1035–1044.

[27] B. Shirdel, M.A. Behnajady, Sol-gel synthesis of Ba-doped ZnO nanoparticles with enhanced photocatalytic activity in degrading Rhodamine B under UV-A irradiation, *Optik* 147 (2017) 143–150.

[28] M.A. Ahmed, M.F.A. Messih, E.F. El-Sherbeny, S.F. El-Hafez, A.M.M. Khalifa, Synthesis of metallic silver nanoparticles decorated mesoporous SnO<sub>2</sub> for removal of methylene blue dye by coupling adsorption and photocatalytic processes, *J. Photochem. Photobiol. A* 346 (2017) 77–88.

[29] M.A. Alvi, A.A. Al-Ghamdi, M. ShaheerAkhtar, Synthesis of ZnO nanostructures via low temperature solution process for photocatalytic degradation of rhodamine B dye, *Mater. Lett.* 204 (2017) 12–15.

[30] X. Zhang, Q. Wang, J. Zhang, J. Wang, M. Guo, S. Chen, C. Li, C. Hu, Y. Xie, One step hydrothermal synthesis of CeO<sub>2</sub>-ZrO<sub>2</sub> nanocomposites and investigation of the morphological evolution, *RSC Adv.* 5 (2015) 89976–89984.

[31] S. Shao, A.-W. Shi, C.-L. Liu, R.-Z. Yang, W.-S. Dong, Hydrogen production from steam reforming of glycerol over Ni/CeZrO catalysts, *Fuel Process Technol* 125 (2014) 1–7.

[32] G. Kresse, J. Furthmüller, Efficient iterative schemes for ab initio total-energy calculations using a plane-wave basis set, *Phys. Rev. B* 54 (1996) 11169–11186.

[33] G. Kresse, J. Furthmüller, Efficiency of ab-initio total energy calculations for metals and semiconductors using a plane-wave basis set, *Comp. Mater. Sci.* 6 (1996) 15–50.

[34] J.P. Perdew, K. Burke, M. Ernzerhof, Generalized gradient approximation made simple, *Phys. Rev. Lett.* 77 (1996) 3865–3868.

[35] L. Ma, G. Wang, C. Jiang, H. Bao, Q. Xu, Synthesis of core-shell TiO<sub>2</sub>@g-C<sub>3</sub>N<sub>4</sub> hollow microspheres for efficient photocatalytic degradation of rhodamine B under visible light, *Appl. Surf. Sci.* 430 (2018) 263–272.

[36] S.G. Kumar, K.S.R.K. Rao, Comparison of modification strategies towards enhanced charge carrier separation and photocatalytic degradation activity of metal oxide semiconductors (TiO<sub>2</sub>, WO<sub>3</sub> and ZnO), *Appl. Surf. Sci.* 391 (2017) 124–148.

[37] Y.-X. Wang, S.-L. Chou, H.-K. Liu, S.-X. Dou, Reduced graphene oxide with superior cycling stability and rate capability for sodium storage, *Carbon* 57 (2013) 202–208.

[38] Q. Zhang, S. Zhang, Y. Tian, S. Zhan, Ce-directed double-layered nanosheet architecture of NiFe-Based hydroxide as highly efficient water oxidation electrocatalyst, *ACS Sustain. Chem. Eng.* 6 (2018) 15411–15418.

[39] C. Zang, X. Zhang, S. Hu, F. Chen, The role of exposed facets in the Fenton-like reactivity of CeO<sub>2</sub> nanocrystal to the orange II, *Appl. Catal. B* 216 (2017) 106–113.

[40] D. Kang, X. Yu, M. Ge, Morphology-dependent properties and adsorption performance of CeO<sub>2</sub> for fluoride removal, *Chem. Eng. J.* 330 (2017) 36–43.

[41] Y. Li, J. Zhu, R. Shi, M. Dirican, P. Zhu, C. Yan, H. Jia, J. Zang, J. He, X. Zhang, Ultrafine and polar ZrO<sub>2</sub>-laid porous nitrogen-doped carbon nanofiber as efficient polysulfide absorbent for high-performance lithium-sulfur batteries with long lifespan, *Chem. Eng. J.* 349 (2018) 376–387.

[42] X. Jia, X. Zhang, N. Rui, X. Hu, C.-j. Liu, Structural effect of Ni/ZrO<sub>2</sub> catalyst on CO<sub>2</sub> methanation with enhanced activity, *Appl. Catal. B* 244 (2019) 159–169.

[43] X. Bu, Y. Gao, S. Zhang, Y. Tian, Amorphous cerium phosphate on P-doped Fe<sub>2</sub>O<sub>3</sub> nanosheets for efficient photoelectrochemical water oxidation, *Chem. Eng. J.* 355 (2019) 910–919.

[44] S.-j. Liu, F.-t. Li, Y.-l. Li, Y.-j. Hao, X.-j. Wang, B. Li, R.-h. Liu, Fabrication of ternary g-C<sub>3</sub>N<sub>4</sub>/Al<sub>2</sub>O<sub>3</sub>/ZnO heterojunctions based on cascade electron transfer toward molecular oxygen activation, *Appl. Catal. B* 212 (2017) 115–128.

[45] W.Y. Teoh, J.A. Scott, R. Amal, Progress in heterogeneous photocatalysis: from classical radical chemistry to engineering nanomaterials and solar reactors, *J. Phys. Chem. Lett.* 3 (2012) 629–639.

[46] J. Di, J. Xia, M. Ji, S. Yin, H. Li, H. Xu, Q. Zhang, H. Li, Controllable synthesis of Bi<sub>4</sub>O<sub>5</sub>Br<sub>2</sub> ultrathin nanosheets for photocatalytic removal of ciprofloxacin and mechanism insight, *J. Mater. Chem. A* 3 (2015) 15108–15118.

[47] M. Wang, M. You, P. Guo, H. Tang, C. Lv, Y. Zhang, T. Zhu, J. Han, Hydrothermal synthesis of Sm-doped Bi<sub>2</sub>MoO<sub>6</sub> and its high photocatalytic performance for the degradation of Rhodamine B, *J. Alloys Compd.* 728 (2017) 739–746.

[48] Y. Li, S. Ouyang, H. Xu, X. Wang, Y. Bi, Y. Zhang, J. Ye, Constructing solid-gas-interfacial fenton reaction over alkalinized-C<sub>3</sub>N<sub>4</sub> photocatalyst to achieve apparent quantum yield of 49% at 420 nm, *J. Am. Chem. Soc.* 138 (2016) 13289–13297.

[49] J.M. Buriak, P.V. Kamat, K.S. Schanze, Best practices for reporting on heterogeneous photocatalysis, *ACS Appl. Mater. Interfaces* 6 (2014) 11815–11816.

[50] S. Wang, X. Hai, X. Ding, K. Chang, Y. Xiang, X. Meng, Z. Yang, H. Chen, J. Ye, Light-switchable oxygen vacancies in ultrafine Bi<sub>2</sub>O<sub>3</sub>-Br nanotubes for boosting solar-driven nitrogen fixation in pure water, *Adv. Mater.* 29 (2017).

[51] H.-P. Jing, C.-C. Wang, Y.-W. Zhang, P. Wang, R. Li, Photocatalytic degradation of methylene blue in ZIF-8, *RSC Adv.* 4 (2014) 54454–54462.

[52] A.G. Trovo, R.F. Nogueira, A. Aguera, A.R. Fernandez-Alba, C. Sirtori, S. Malato, Degradation of sulfamethoxazole in water by solar photo-Fenton. Chemical and toxicological evaluation, *Water Res.* 43 (2009) 3922–3931.

[53] X. Liu, X. Zhang, K. Shao, C. Lin, C. Li, F. Ge, Y. Dong, Fe<sub>0</sub>-activated persulfate-assisted mechanochemical destruction of expired compound sulfamethoxazole tablets, *RSC Adv.* 6 (2016) 20938–20948.

[54] L. Hu, P.M. Flanders, P.L. Miller, T.J. Strathmann, Oxidation of sulfamethoxazole and related antimicrobial agents by TiO<sub>2</sub> photocatalysis, *Water Res.* 41 (2007) 2612–2626.

[55] M.N. Abellán, B. Bayarri, J. Giménez, J. Costa, Photocatalytic degradation of sulfamethoxazole in aqueous suspension of TiO<sub>2</sub>, *Appl. Catal. B* 74 (2007) 233–241.

[56] C. Qi, X. Liu, C. Lin, X. Zhang, J. Ma, H. Tan, W. Ye, Degradation of sulfamethoxazole by microwave-activated persulfate: kinetics, mechanism and acute toxicity, *Chem. Eng. J.* 249 (2014) 6–14.

[57] M.S. Sher Shah, A.R. Park, K. Zhang, J.H. Park, P.J. Yoo, Green synthesis of biphasic TiO<sub>(2)</sub>-reduced graphene oxide nanocomposites with highly enhanced photocatalytic activity, *ACS Appl. Mater. Interfaces* 4 (2012) 3893–3901.

[58] P.V. Kamat, Graphene-based nanoassemblies for energy conversion, *J. Phys. Chem. Lett.* 2 (2011) 242–251.

[59] W.K. Jo, N. Clément Sagaya Selvam, Enhanced visible light-driven photocatalytic performance of ZnO-g-C<sub>3</sub>N<sub>4</sub> coupled with graphene oxide as a novel ternary nanocomposite, *J. Hazard. Mater.* 299 (2015) 462–470.

[60] H. Tian, H. Fan, J. Ma, Z. Liu, L. Ma, S. Lei, J. Fang, C. Long, Pt-decorated zinc oxide nanorod arrays with graphitic carbon nitride nanosheets for highly efficient dual-functional gas sensing, *J. Hazard. Mater.* 341 (2018) 102–111.